Appendix for

Solution-driven processing of calcium sulfate: the mechanism of the reversible transformation of gypsum to bassanite in brines

Tomasz M. Stawski*[1], Stephanos Karafiludis[×1,2], Carlos Pimentel[×3], German Montes-HernándezMontes Hernandez[3], Zdravko Kochovski[4], Ralf Bienert[1], Karin Weimann[1], Franziska Emmerling[1,2], Ernesto Scoppola[5], Alexander E. S. Van Driessche**[6]

1. Federal Institute for Materials Research and Testing (BAM), Richard-Willstätter-Straße 11, 12489 Berlin, Germany
2. Department of Chemistry, Humboldt-Universität zu Berlin, Brook-Taylor-Straße 2, 12489 Berlin, Germany;
3. Univ. Grenoble Alpes, Univ. Savoie Mont Blanc, CNRS, IRD, Univ. Gustave Eiffel, ISTerre, 38000 Grenoble, France;
4. Helmholtz-Zentrum Berlin for Materials and Energy, Hahn-Meitner Platz 1, 14109 Berlin, Germany;
5. Biomaterials, Hierarchical Structure of Biological and Bio-inspired Materials, Max Planck Institute of Colloids and Interfaces, Potsdam 14476, Germany;
6. Instituto Andaluz de Ciencias de la Tierra (IACT), CSIC – Universidad de Granada, Av. De las Palmeras 4, 18100 Armilla, Spain;

Tomasz M. Stawski: https://orcid.org/0000-0002-0881-5808;
Stephanos Karafiludis: https://orcid.org/0000-0002-7257-6311 ;
Carlos Pimentel: https://orcid.org/0000-0002-5400-9102;
German Montes Hernandez https://orcid.org/0000-0002-8655-6530;
Zdravko Kochovski: https://orcid.org/0000-0001-8375-0365 ;
Ralf Bienert: https://orcid.org/0000-0003-2324-3403;
Karin Weimann: https://orcid.org/0009-0002-5727-3459;
Franziska Emmerling: https://orcid.org/0000-0001-8528-0301;
Ernesto Scoppola: https://orcid.org/0000-0002-6390-052X;
Alexander E. S. Van Driessche https://orcid.org/0000-0003-2528-3425;

*tomasz.stawski@bam.de; **alexander.vd@csic.es

[×] These authors contributed equally

Materials and Methods

Synthesis

Na_2SO_4 (ChemSolute, 99%), $CaCl_2 \cdot 2H_2O$ (ChemSolute, 99%) and NaCl (ChemSolute, 99%) were used in our experiments. We prepared NaCl solutions at a required concentration (0.4 M - 4.8 M) by dissolving the calculated amount of salt in deionised water (> 18 MΩ·cm). The Ca^{2+} and SO_4^{2-} stock solutions were prepared by dissolving the calculated amount of salt in a NaCl brine solution. In the experiments involving natural gypsum, we used 0.2 M $CaSO_4$ equivalent solutions/slurries, which contained 34.4 g/L of dispersed natural gypsum powder (M_m = 172.17 g/mol) and 4.8 M of NaCl.

Thermodynamic calculations

We obtained the solubility values of different calcium sulfate phases as a function of temperature for various salinity conditions by performing thermodynamic modelling. The values were calculated with PHREEQC 2(Parkhurst and Appelo, 1999) and the included Pitzer database. and with PHREEQC 3(Parkhurst and Appelo, 2013) with an updated Pitzer database (Eq. S1). In PHREEQC code, the solubility product of the different phases can be given in three different ways, the simplest being the solubility product at T = 25 °C, which is provided for all phases. However, the solubility is temperature-dependent and, to take this fact into account, two other methods of calculating the solubility product can be used: the Van't Hoff equation or the analytical Pitzer expression (Eq. S1)

$$log_{10} K = A1 + \frac{A2}{T} + \frac{A3}{T} + A4\, log_{10} T + \frac{A5}{T^2} + A6T^2 \qquad \textbf{Eq. S1}$$

In Eq. S1 up to 6 coefficients (A1-A6) can be included in the database to determine the solubility product at the specified temperature T (in K). This expression, which is preferably used by PHREEQC to calculate the solubility product, cannot always be used, as not all phases have A-constants provided.

The differences observed in the calculation of the solubility of gypsum and anhydrite using PHREEQC 2 and PHREEQC 3 are resulting from the different coefficients used to define the solubility products of these phases in the Pitzer databases, as we compare in Table S1.

In addition to this difference in the parameters used to calculate the solubility products in Table S1, the two versions of PHREEQC contain different parameters of the ionic interactions in solution for the aqueous Pitzer model and the parameters for determining the molar volumes of the ions in solution. Hence, when using the same analytical parameters for bassanite, extracted from the included LLNL (Lawrence Livermore National Laboratory) database, the solubilities obtained are different when calculated with PHREEQC 2 and 3.

Flow-through setup for scattering

All the scattering experiments were performed using a PEEK flow-through cell coupled with a pump setup to a 100 mL glass reactor. The reactor was placed on a computer-controlled integrated heating and magnetic stirring plate (IKA RCT Digital), and was equipped with a reflux condenser to prevent evaporation of solutions. The heat was transferred from the hot plate to the reactor with an aluminium mantle, and the feedback thermocouple was inserted directly into the solution-containing reactor. The heating profiles were programmed with a custom Python-script, which controlled the hot plate and recorded actual measured profiles. The profiles were synchronised with scattering data frames, against time and temperature . At the beginning of an experiment, 25 mL of 0.4 M $CaCl_2$ stock solution in 4.4 M NaCl brine was equilibrated at a given starting temperature and stirred at 1000 rpm. The content of the reactor was continuously circulated through a borosilicate glass capillary cell (ID = 1.498 mm) using a peristaltic pump (Longer BT100-2J) at 300 mL/min. To obtain calcium sulfate, 25 mL of a 0.4 M Na_2SO_4 in 4.4 M NaCl brine solution was injected into the reactor at 300 mL/min using a second peristaltic pump with a remote control. The injected solution was also equilibrated at a required temperature, before the injection. The dead volume of tubing was ~5 mL. We used the same setup to measure the scattering from pure water and 4.4 - 4.8 M NaCl brine solutions, at 25 °C < T < 95 °C, which we needed as reference and backgrounds. This was done by using a temperature programme with 1 °C steps.

Synchrotron-based scattering

X-ray scattering measurements were performed on the mySpot beamline(Zizak, 2016) of BESSY-II (Helmholtz-Zentrum Berlin, HZB, Germany), using a monochromatic X-ray beam at 18.0 keV aligned with a capillary of the flow-through setup. Scattered intensities, small- and wide-angle X-ray scattering (SAXS/WAXS) were collected with a large-area Dectris Eiger 9M detector as a single continuous signal. We typically measured with 10 s or 20 s time resolution, depending on an experiment. The sample-to-detector distance of ~330 mm allowed for a usable q-range of ~0.1 < q < 39 nm^{-1} . Transmission through the sample was calculated using an X-ray fluorescence signal collected from a lead beamstop using a RAYSPEC Sirius SD-E65133-BE-INC detector equipped with an 8 μm beryllium window, where the incoming beam intensity was monitored and normalised using an ion chamber. The scattering q-range was calibrated against silicon (NIST SRM640) and the corresponding measured intensity was calibrated to absolute units against water (at various temperatures) and a glassy carbon standard (NIST SRM3600, 1 mm, at T = 20 ℃). The resulting data were processed with custom Python scripts utilizing a pyfai library(Ashiotis et al., 2015). The processing steps included angle-dependent integration to 1D scattering curves and subtraction of an instrumental background (i.e. an “empty beamline” or “air” background). The 2D scattering patterns showed two anisotropic directions: meridian (N-S), and equatorial (W-E) (Fig. S2). The direction-dependent scattering curves were obtained by performing integrations in the opposite quadrants (0° at E) : N +45°, +135°, S +225°, -45°; and E -45°,+45° with W 135°, 225°. The rationale for the analysis in presented in the next section.

The resulting scattering data were corrected for transmission and scaled to absolute intensity units. The as-obtained raw scattering curves were further corrected for scattering of the capillary cell containing a brine solution. The data from the evolving calcium sulfate solutions were always matched against brine backgrounds for a given temperature with an accuracy of 1 °C, based on the recorded temperature profiles. This was a crucial correction because scattering profiles of aqueous solutions are strongly affected by temperature. The beam profile was also measured to account for the instrumental effects onto the diffraction peaks’ parameters. This was performed by scanning the beam

vertically and horizontally across two perpendicular 0.1 mm tungsten wires. The diffraction peaks were separated from the scattering data by applying an Asymmetric Least Square Smoothing baseline correction method(Eilers and Boelens, 2005; Peng et al., 2010), and selected characteristic peaks were fitted with pseudo-Voigt functions convoluted with the beam profile to extract information about their positions, broadening values and areas as a function of time.

Data analysis and the scattering model

One important aspect is that as the calcium sulfate crystals evolve, they exhibit orientation-dependent anisotropic 2D intensity profiles (Fig. S3). This phenomenon is a characteristic feature of the calcium sulfate system when characterized using a flow-through capillary(Stawski et al., 2019, 2016). Specifically, both gypsum and bassanite primarily form acicular single crystals(Stawski et al., 2019). As the crystals reach sizes of a few hundreds nanometers to several micrometers, they align themselves with the flow along their long-axes as they pass through a horizontally mounted capillary. This leads to a texture in an otherwise polycrystalline system (Fig. S3, Fig. S4). Additionally, at small-angles and at length-scales >>1 nm, a texture is also observable because calcium sulfate single crystals are internally mesostructured(Besselink et al., 2016; Stawski et al., 2021, 2019), meaning that they consist of slightly misaligned crystallographic domains, resembling brick-in-the-wall-like units. The direction-dependent intensity variations were clearly observable for the diffraction rings (wide-angle scattering, WAXS), as well as for the scattering around the beamstop in the center (small-angle scattering, SAXS) (Fig. S3,: Fig. S4). The extent of the anisotropy evolved with time following the temperature profile and is related to the changes in crystal phase, size, and morphology (Fig. S4). Therefore, the analysis of orientation-dependent changes in intensity and the crystal morphology of calcium sulfate provides valuable insights into the crystallisation mechanisms, which is discussed in the main text.

The small-angle scattering data for selected directions of in integration, were fitted with a model based on a unified equation by Beaucage et al. for two structural levels(Beaucage, 1995) (Eq. S2).

$$I(q) \simeq Gexp\left(-\frac{q^2R_g^2}{3}\right) + Bexp\left(-\frac{q^2R_s^2}{3}\right)\left(\frac{\left[erf(qR_g/\sqrt{6})\right]^3}{q}\right)^D + \\ +G_sexp\left(-\frac{q^2R_s^2}{3}\right) + B_s\left(\frac{\left[erf(qR_s/\sqrt{6})\right]^3}{q}\right)^P + bkg$$ **Eq. S2**

Here, G, B, G_s, and B_s are prefactors, D and P are scattering exponents, and R_g and R_s are radii of gyration of the characteristic length-scales, *bkg* is a background constant and *erf* is an error function. For the case of our dataset, Eq. S2 can be further simplified. In all our experiments at low q the intensity follows a q^{-D} dependence, that implies that $R_g \rightarrow \infty$. For such a limit, we obtain Eq. S3, rendering effectively a "1.5-level model". The smaller building units of a radius of gyration R_s are assumed to be simply sphere-like, thus $P = 4$, as one would expect for a terminal high-q region.

$$I(q) \simeq Bexp\left(-\frac{q^2R_s^2}{3}\right)\left(\frac{1}{q}\right)^D + G_sexp\left(-\frac{q^2R_s^2}{3}\right) + B_s\left(\frac{\left[erf(qR_s/\sqrt{6})\right]^3}{q}\right)^P + bkg$$ **Eq. S3**

In Fig. S5 we show a fit with Eq. S3 to a selected dataset, and the individual contributions of the B-, G_s- and B_s - dependent components.

In situ Raman spectroscopy

In situ Raman spectroscopy was performed to monitor the sequence of phases occurring during gypsum bassanite cycling and to determine the concentration of dissolved sulfate. For this purpose, 100 mL of 0.4 M $CaCl_2$ and 4.4 M NaCl was directly mixed with 100 mL of 0.4 M Na_2SO_4 and 4.4 M NaCl in a custom-built hydrothermal reactor with temperature control and continuously stirred (400 pm). The experiment with 0.4 M NaCl was performed by adding 100 mL of 0.4 M $CaCl_2$ to 100 mL of 0.4 M Na_2SO_4. In the case of natural gypsum 300 mL of 34.4 g/L of dispersed natural gypsum powder (M_m = 172.17 g/mol) and 4.8 M of NaCl was placed in the reactor and continuously stirred (300 rpm). The reactor is equipped with a 785 nm infrared laser, with which Raman spectra were recorded from 100 to 3425 cm^{-1} using a RAMAN RXN1 spectrometer from Kaiser Optical Systems (Ann Arbor, USA). Spectra were averaged over three scans of 15 s with a time interval of 60 s. A detailed description of the used Raman setup can be found in the literature (Montes-Hernandez and Renard, 2016).

Fourier-transform infrared spectroscopy

Fourier-transform infrared spectroscopy (FTIR) was conducted to acquire spectral data from precipitates formed during the transformation process carried out in unstirred reactors (1.5 mL). In these experiments, a stock solution was prepared by mixing 100 mL of 0.4 M $CaCl_2$ and *X* M NaCl with 100 mL of 0.4 M Na_2SO_4 and *X* M NaCl (where *X* stands for 1 M, 2 M, 3 M, 3.5 M, 4 M and 4.4 M). This stock solution was allowed to react for 24 hours to reach equilibrium between the precipitated gypsum crystals and the solution. After this time, the solution was vigorously stirred to achieve a homogeneous suspension of the gypsum crystals and 1.5 mL of solution was pipetted into each of the reactors. These reactors were heated to T = 90 °C for all experiments, and also to T = 70 °C and T = 80 °C for experiments in which 4.4 M NaCl was added. The crystals were extracted at different time intervals to study the transformation reactions. FTIR analysis was performed in ATR mode (Thermo Scientific Nicolet iS50) to identify the calcium sulfate phases. Dry powder samples were placed on the diamond window. The spectra were evaluated for peak shifts that allowed for the differentiation between bassanite and gypsum.

Cryogenic Transmission Electron Microscopy

The flow-cell experiment, following the conditions in Fig. 3, was reproduced for the electron microscopy investigation. Aliquots of slurries were taken directly from the reactor when gypsum was converted to bassanite at ~4860 s. Cryo-TEM imaging was performed using a JEOL JEM-2100 transmission electron microscope (JEOL GmbH, Eching, Germany). Specimens were prepared by casting a 4 µl droplet of the aliquot solutions onto lacey carbon-coated copper TEM grids (200 mesh, Electron Microscopy Sciences, Hatfield, PA), and plunge-freezed into liquid ethane using an FEI vitrobot Mark IV set at 4 °C and 95% humidity. Vitrified grids were either transferred directly to the microscope's cryo-transfer holder (Gatan 914, Gatan, Munich, Germany) or stored in liquid nitrogen. All grids were glow-discharged before use. Imaging was carried out at temperatures around T = -180 °C. The TEM was operated at an acceleration voltage of 200 kV, and an objective lens defocus of about 1.5–2

μm was used to increase the contrast. Micrographs were recorded with a bottom-mounted 4·4k CMOS camera (TemCam-F416, TVIPS, Gauting, Germany). Each micrograph's electron dose was kept below 20 e/Å^2 to minimise any potential beam damage to the samples. All images were processed using ImageJ2(Rueden et al., 2017).

Supporting Figures

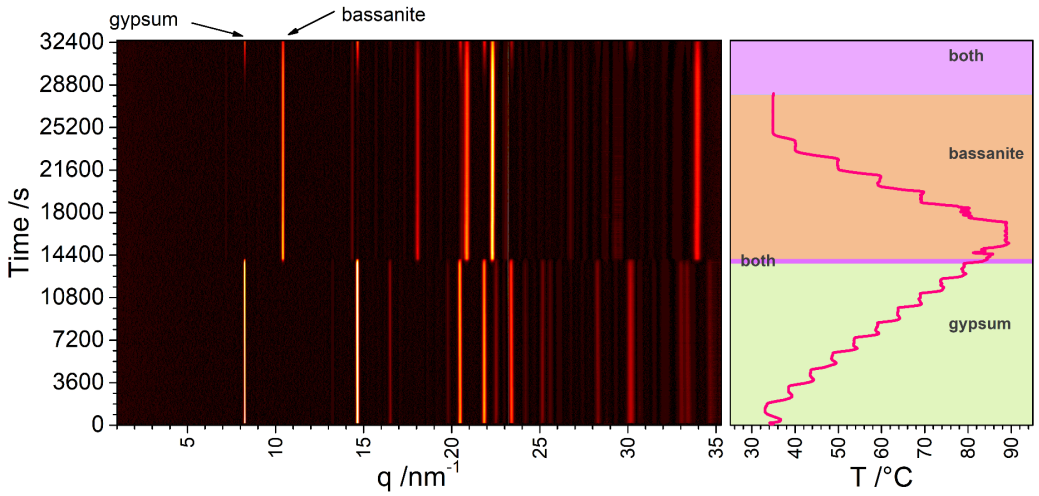

Fig. S1. (left) The *in situ* and time-resolved isotropic diffractogram showing crystalline phases which form in a 0.2 M $CaSO_4$ - 4.8M NaCl aqueous solution upon following a multi-ramp temperature profile (right) over a period of ~9 h. The first characteristic peaks of gypsum (COD 2300259) and bassanite (AMCSD 0006909) are indicated with arrows. The coloured backgrounds are areas where the phases occur:: gypsum (green), bassanite (orange); both phases (purple).

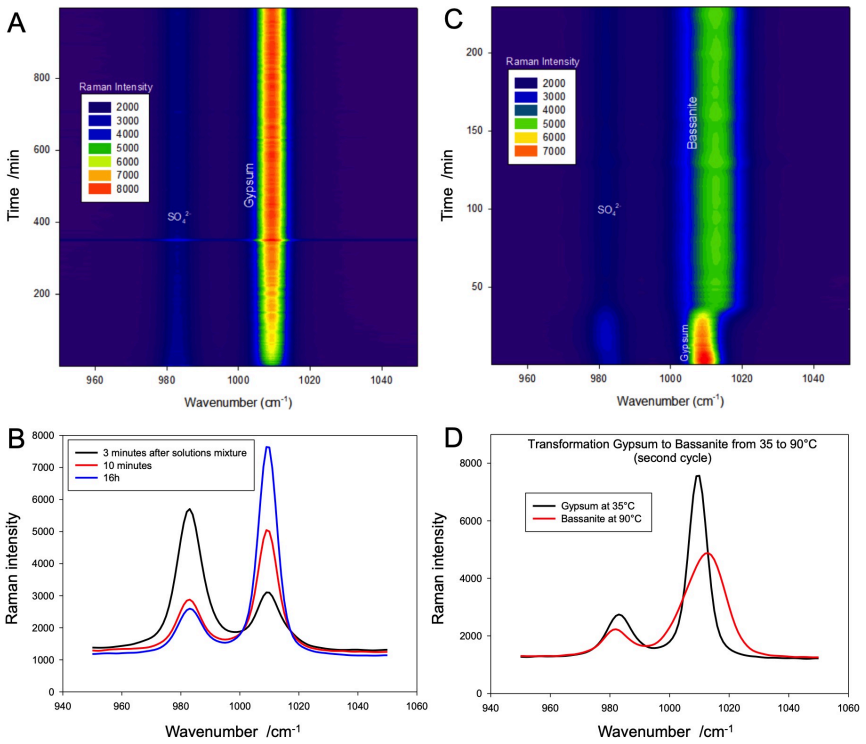

Fig. S2. Time-resolved Raman spectroscopy of gypsum precipitation (A,B) and gypsum to bassanite conversion (C,D). (A) Gypsum precipitation at T = 35 °C from a solution containing 0.2 M $CaSO_4$ and 4.8 M NaCl, selected Raman spectra (B) show that as precipitation proceeds the aqueous sulfate signal decreases and the v1 mode band increases. (C) Bassanite transformation into gypsum when the temperature is lowered to T = 35 °C. This is the 2nd cycle of conversion and is the continuation of the first cycle shown in Fig. 3B.

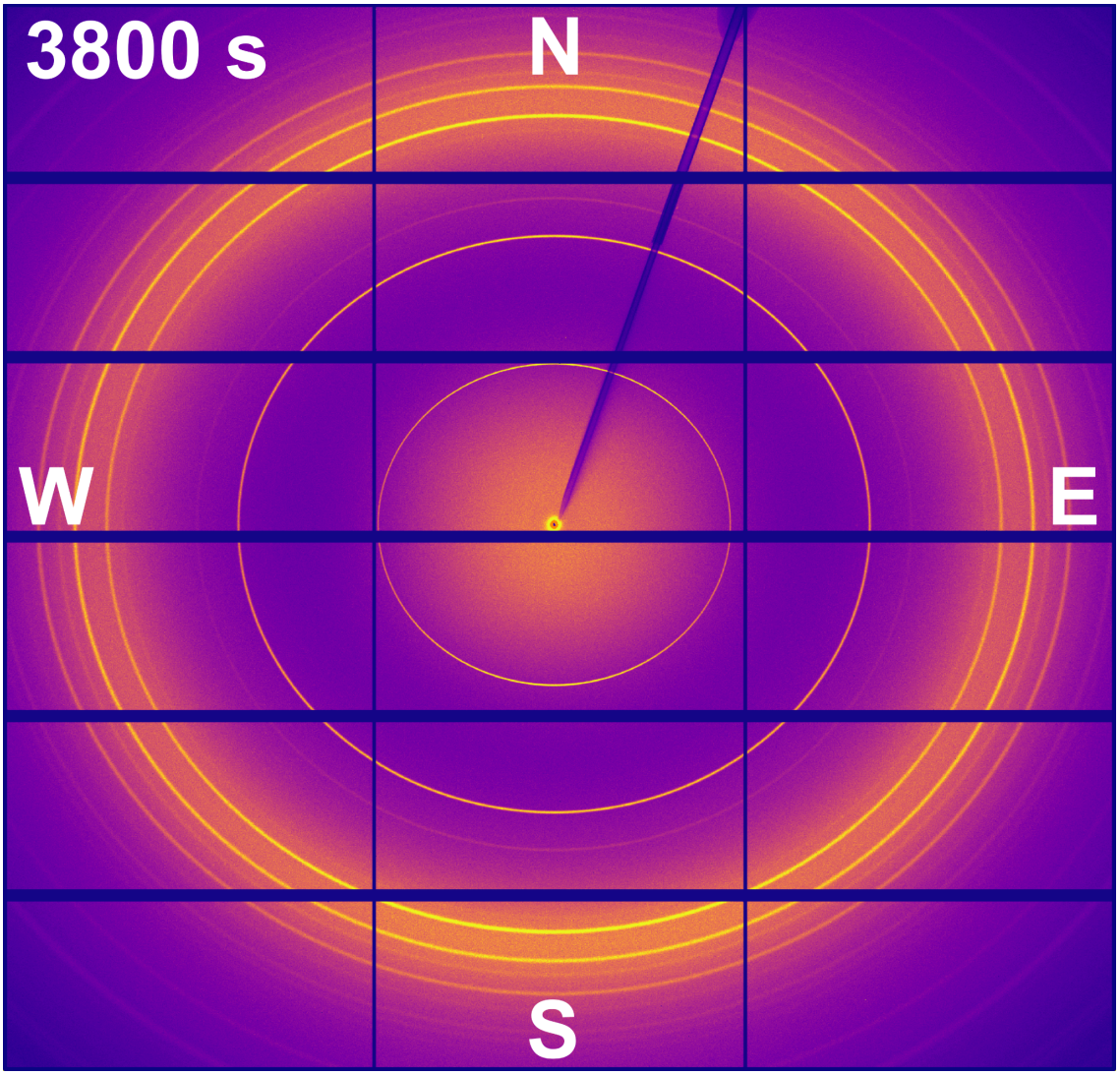

Fig. S3. Selected 2D scattering data frame from phases developing in a 0.2 M $CaSO_4$ - 4.8M NaCl aqueous solution at 3800 s. For the temperature profile and the corresponding times, see Fig. 3 in the main text. The 2D pattern contains contributions from gypsum and bassanite phases. The scattering pattern shows two anistropic directions: meridian (N-S), and equatorial (W-E). The integration to 1D scattering patterns was performed by combining opposite quadrants (0° at E) : N +45°, +135°, S +225°, -45°; and E -45°,+45° with W 135°, 225°.

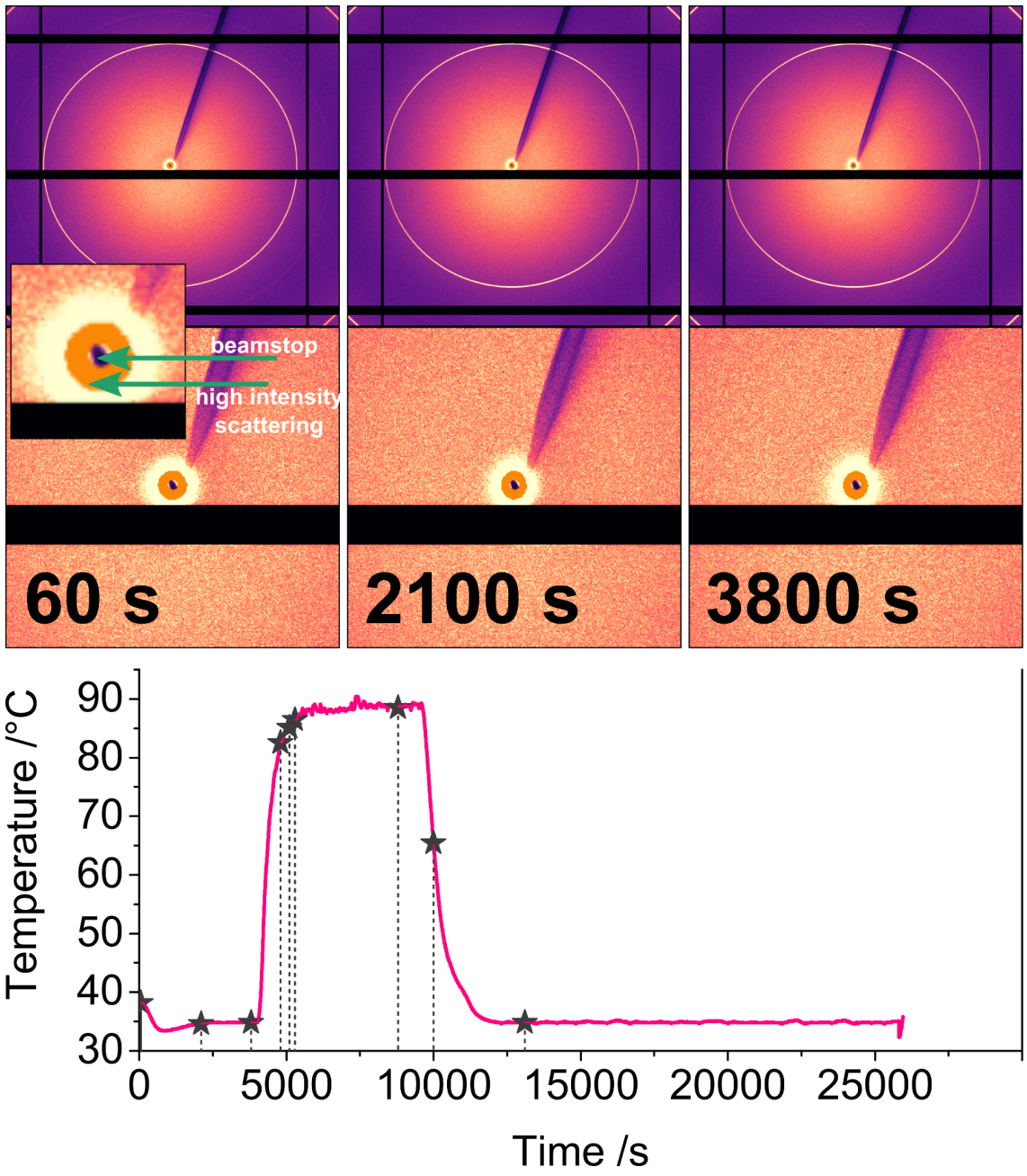

Fig. S4. Selected 2D scattering data frames from phases developing in a 0.2 M $CaSO_4$ - 4.8M NaCl aqueous solution upon following a multi-ramp temperature profile (bottom). The *q*-range of the 2D patterns is trimmed to highlight the first diffraction peaks of either gypsum or bassanite (the upper rows of each time frame), and the small-angle region around the beamstop (the lower rows); the inset at 60 s highlights the beamstop in the centre, which is surrounded by the high intensity in orange. The shape of this particular intensity region clearly evolves with anisotropy. The example of a complete frame is shown in Fig. S3[OBJ]. The frames were selected based on the reaction temperature profile (bottom), in which consequent time points corresponding to the frames are marked with stars. Part 1/3.

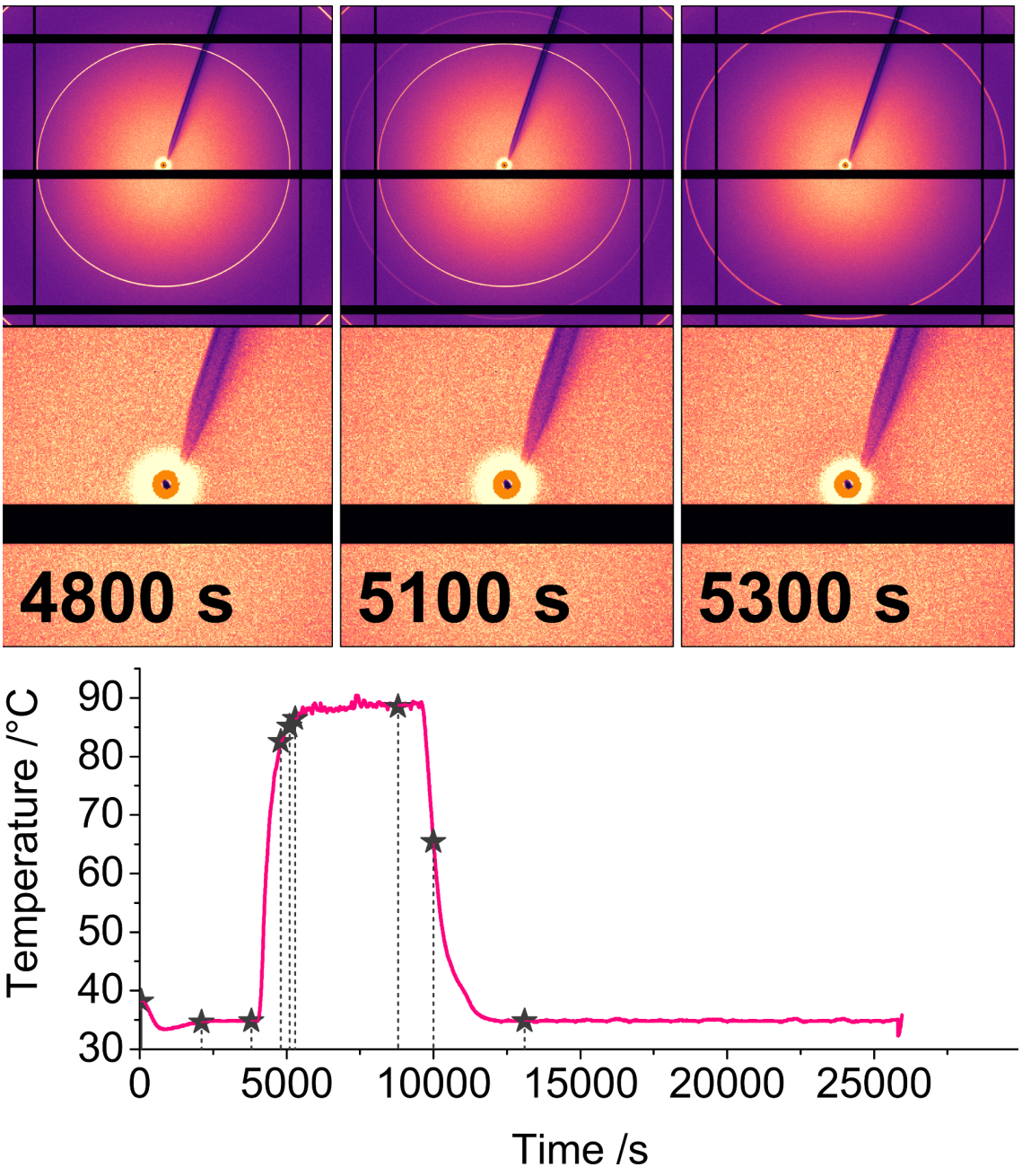

Fig. S4. Continued. Part 2/3.

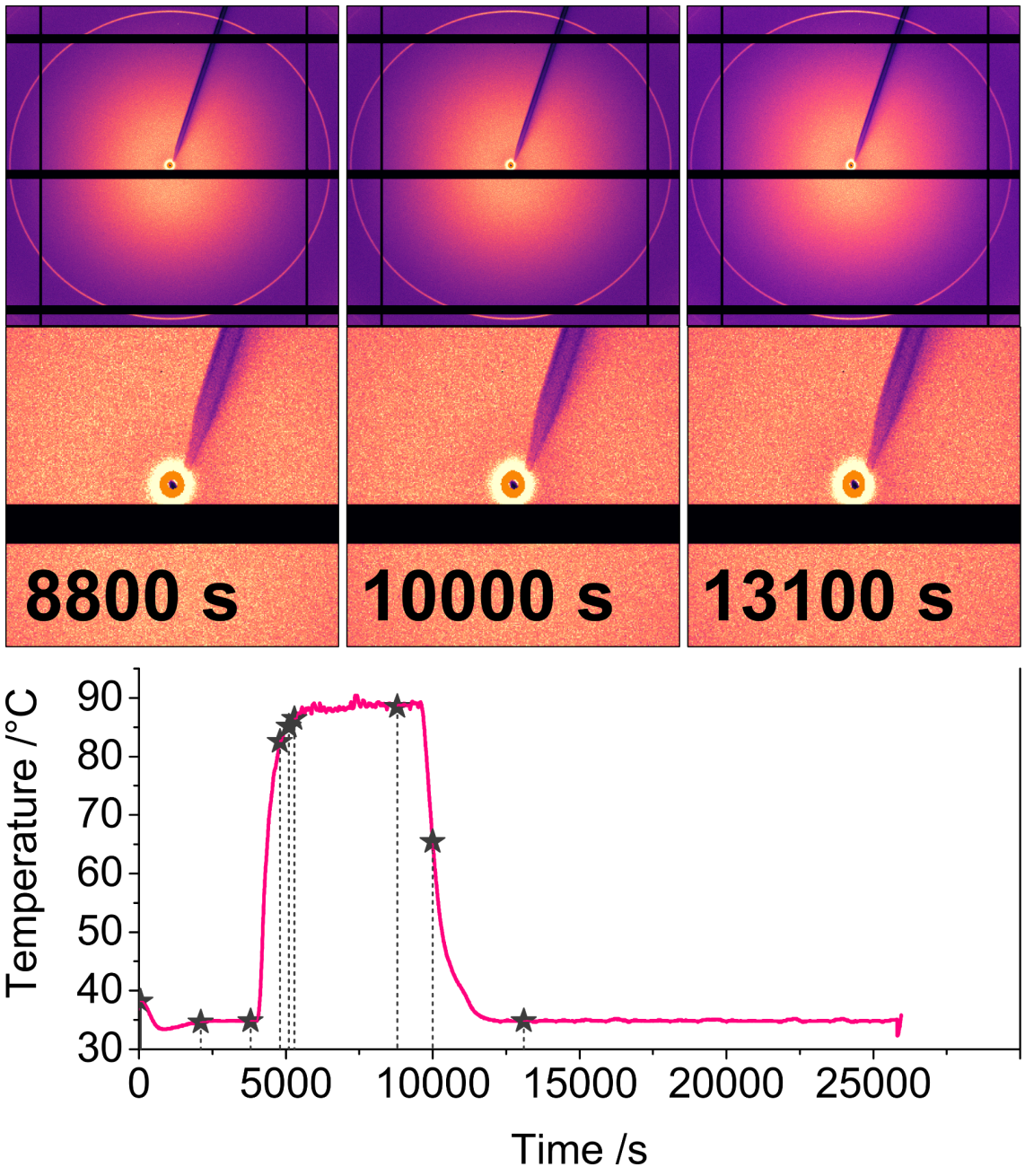

Fig. S4. Continued. Part 3/3.

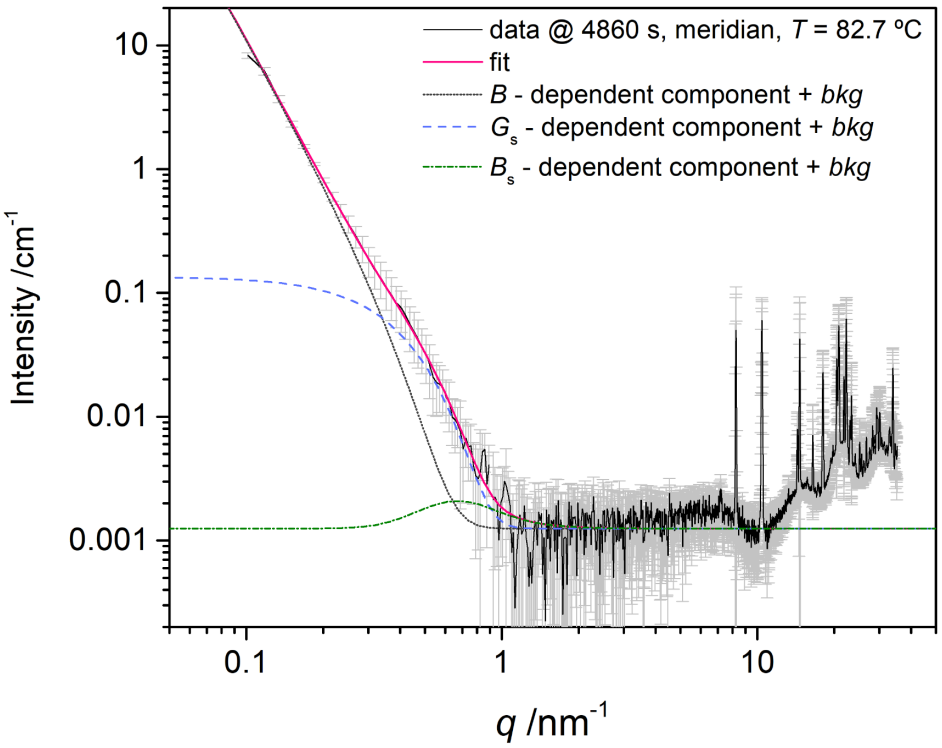

Fig. S5. Selected scattering data at 4860 s (T = 83 °C) for the signal in the meridian direction, together with a fit with Eq. S3. The contributions of the individual components in the equation are also plotted. The model was fitted for 0.1 nm^{-1} < q < 3 nm^{-1}, and the fitted curves are extrapolated beyond this range. B = 0.00263 ± 3.11734E-4 cm^{-1}; D = 3.64489 ± 0.06552; G_s = 0.13421 ± 0.03174 cm^{-1}; B_s = 4.72714E-4 ± 2.17781E-4 cm^{-1}; R_s = 4.49913 ± 0.23052 nm; *bkg* = 0.00125 ± 4.67886E-5 cm^{-1}.

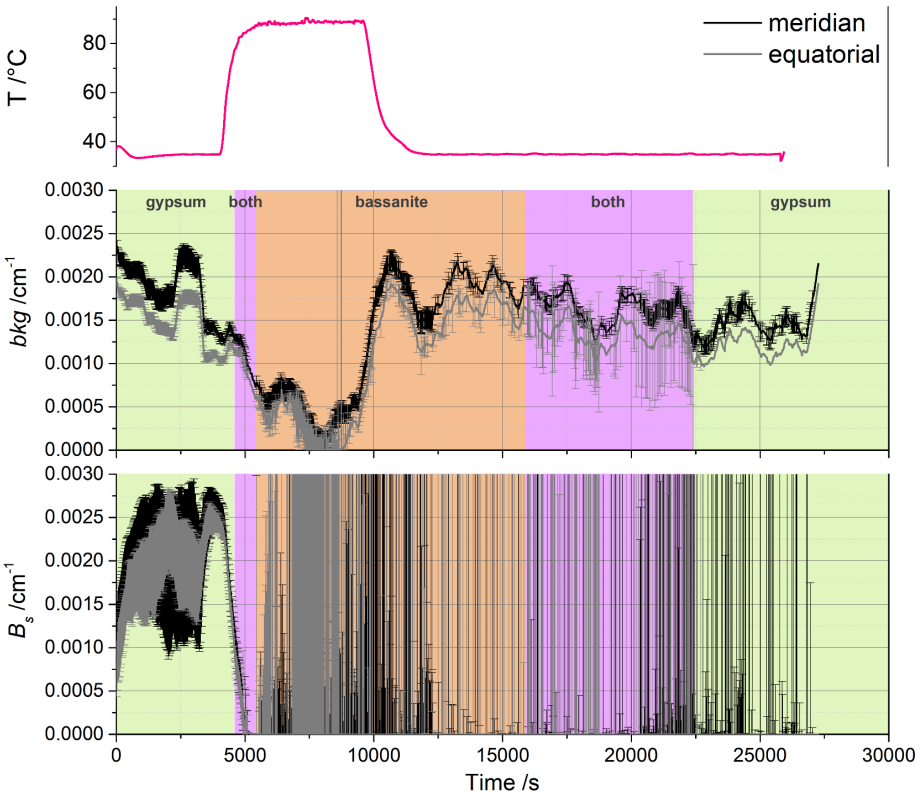

Fig. S6. The evolution of the fitting B_s and *bkg fitting* parameters derived for the model in Eq. S3, which characterise the small-angle scattering data. See also Fig. S5. The temperature profile is included for reference. The coloured backgrounds are areas where the phases occur:: gypsum (green), bassanite (orange); both phases (purple).

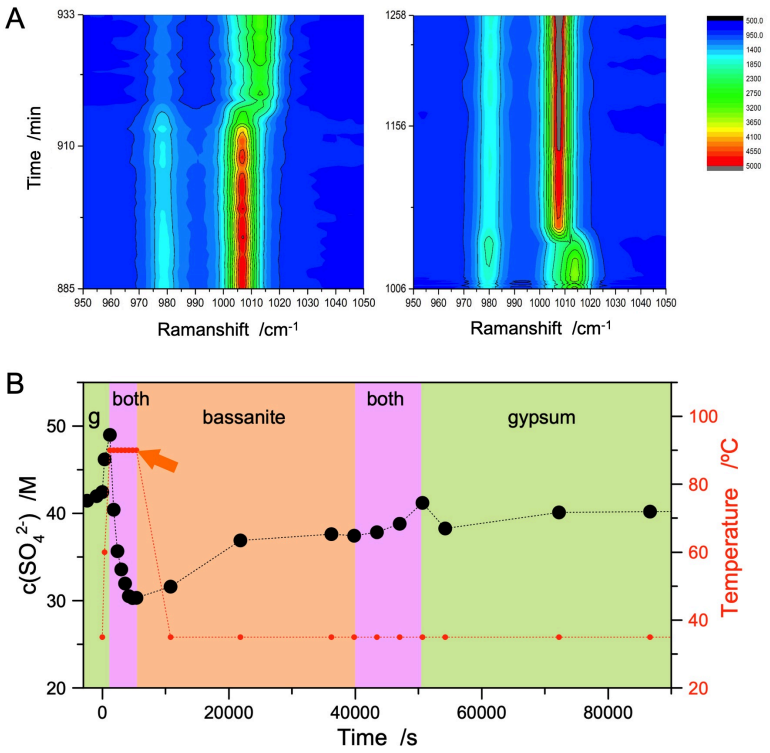

Fig. S7. Colour plots displaying Raman spectra intensity variation over time for gypsum, bassanite and aqueous sulfate (only the zone of interest between 950 and 1050 cm^{-1} is shown) during the conversion of natural gypsum to bassanite. (A) Left: Natural gypsum equilibrating in a solution of 4.8 M NaCl (only the last 1800 s are shown). Equilibration is so fast that actually all dissolution of gypsum took place before the reactor could be assembled. Right: Full cycle of gypsum-bassanite-gypsum conversion. (B) Aqueous sulfate concentration profile during the conversion of natural gypsum to bassanite as a function of temperature. Prior to 0 s the gypsum suspension had been equilibrating for > 84000 s at RT (a). The orange arrow indicates the peak in aqueous sulfate concentration at the onset of gypsum to of bassanite transformation. The coloured backgrounds are areas where the phases occur:: gypsum (green), bassanite (orange); both phases (purple).

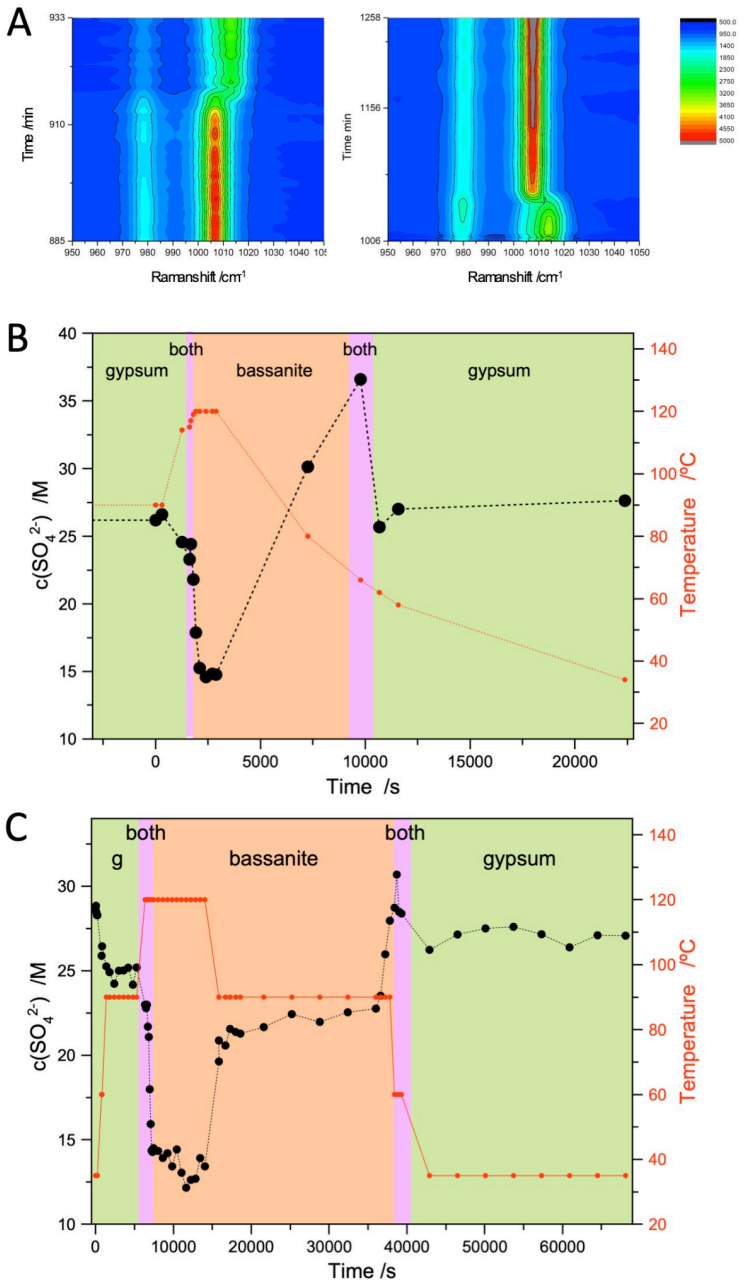

Fig. S8. Time-resolved Raman spectroscopy monitoring of a gypsum-bassanite-gypsum conversion cycle at low salinity, 0.4 M NaCl. (A) Colour plots displaying Raman spectra intensity variation over time for precipitates and aqueous sulfate. (B) Aqueous sulfate concentration evolution during gypsum-bassanite-gypsum conversion. Before 0 s the gypsum suspension had been equilibrating for >86499 s (1 day) at T = 35 °C, and then 50400 s at T = 90 °C. The experiment began at T = 35 °C, allowing the 0.2 M $CaSO_4$ equivalent solution to equilibrate for several days. The temperature was then increased to T = 90 °C, with no changes observed in the Raman spectra, which indicated that gypsum was the only persistent phase at this temperature. Under these conditions, dissolved sulfate concentration stabilized at ~26 mM. Subsequently, the temperature was increased to T = 120 °C (thus under hydrothermal conditions), and bassanite started to form when the temperature reached T = 115 °C, 1380 s (relative) after starting heating. This was accompanied by a drop in the free sulfate

concentration from 26 mM to 14 mM. When the temperature was lowered to T = 80 °C, bassanite remained the only phase, but an increasing free sulfate concentration indicated that bassanite was already dissolving. 2520 s (relative) later, at a temperature of T = 60 °C (, gypsum had started to form and bassanite disappeared completely 900 s later, as the temperature reached T = 60 °C. This total conversion was characterized by a sharp decrease in sulfate concentration (~26 to 14 mM). When the slurry reached T = 35 °C, the sulfate concentration increased slightly to (27.5 mM). (C) Aqueous sulfate concentration evolution during gypsum-bassanite-gypsum conversion with long equilibration time at T = 120 °C and T = 90 °C. Once the solution temperature is lowered below T = 90 ºC, bassanite starts to convert rapidly to gypsum. The coloured backgrounds are areas where the phases occur:: gypsum (green), bassanite (orange); both phases (purple).

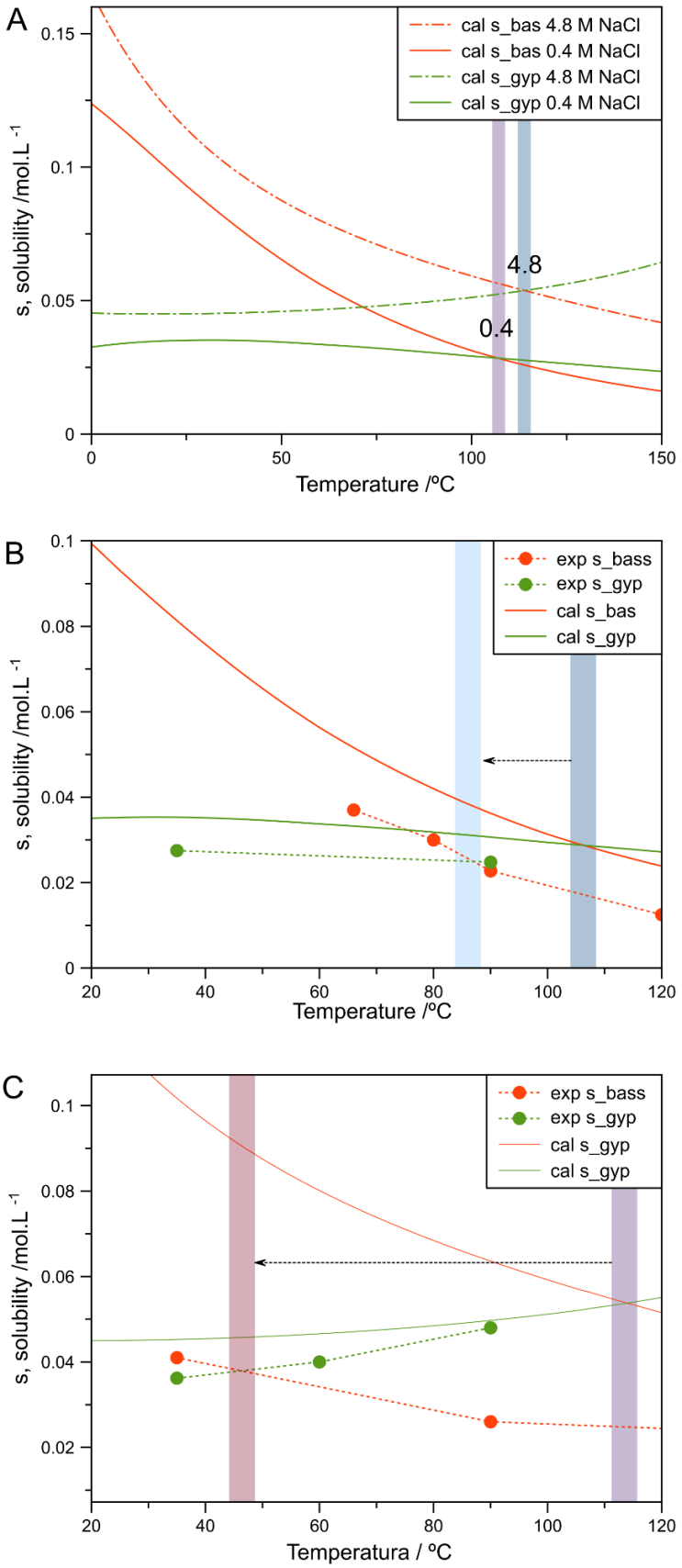

Fig. S9. Gypsum and bassanite solubility crossover. A) PHREEQC 3 solubility data for bassanite (orange) and gypsum (green) are shown at 0.4 and 4.8 M NaCl. At low salinity the

thermoddemV1 database was used, while in the case of high salinity the Pitzer database was used. The solubility crossover is predicted to shift to higher temperatures with increasing salt concentration, as indicated by the shaded purple (0.4 M NaCl) and blue (4.8 M NaCl) bands, which indicate the crossover points. B) Experimentally determined sulfate concentrations (coloured dots) of solutions containing 0.4 M NaCl in contact with gypsum and bassanite at different temperatures are shown. The black arrow between the shaded bands highlights the difference in the experimental (light blue) and predicted (dark blue) crossover temperature. C) Experimentally determined sulfate concentrations of solutions containing 4.8 M NaCl in contact with gypsum and bassanite at different temperatures are presented. The experimental and calculated values differ significantly for bassanite, where the calculated solubility is much higher than the measured one. Importantly, the experimental crossover (mauve band) in solubilities occurs at a much lower temperature than predicted (purple band), as indicated by the black arrow.

Supporting Tables

Table S1. Selected analytical coefficients in Eq. S1 for gypsum and anhydrite in the Pitzer database included in PHREEQC 2 and PHREEQC 3 codes.

		A1	A2	A3	A4
gypsum	PHREEQC 2	90.318	0	-4213.0	-32.641
	PHREEQC 3	82.381	0	-3804.5	-29.9952
anhydrite	PHREEQC 2	422.950	0	-18431.0	-147.708
	PHREEQC 3	5.009	-2.21e-2	-796.4	-

Table S2. Transformation times as a function of the hydrodynamic conditions present in the reaction vessel at 1000 rpm (fast stirring, SAXS/WAXS), 400 rpm (slow stirring, in situ Raman), and without stirring derived from ex situ FTIR experiments. The coloured backgrounds are areas where the phases occur:: gypsum (green), bassanite (orange); both phases (purple).

gypsum-to-bassanite

	Fast stirring (1000 rpm)	Slow stirring (400 rpm)	No stirring		
Time /h	90 °C	90 °C	90 °C	80 °C	70 °C
0	gypsum	gypsum	gypsum	gypsum	gypsum
0.25	bassanite	both	gypsum	gypsum	gypsum
0.5		bassanite	gypsum	gypsum	gypsum
1.0			bassanite	gypsum	gypsum
3.0				gypsum	gypsum
4.0				both	gypsum
6.0				bassanite	gypsum
24					gypsum
48					gypsum
120					bassanite

bassanite-to-gypsum

	Fast stirring (1000 rpm)	Slow stirring (400 rpm)
Time /h	35 °C	35 °C
0	bassanite	bassanite
1.0	bassanite	bassanite
2.0	both	bassanite
48	gypsum	bassanite
20		both
24		gypsum
48		gypsum

Table S3. Phases obtained as a function of time and salt concentration. The experiments were carried out at 90 °C using batch reactors. All experiments were conducted by mixing equal volumes of two solutions: 0.4 M $CaCl_2$ in *x* NaCl and 0.4 M Na_2SO4 in *x* NaCl, where X stands for 1 M, 2 M, 3 M, 3.5 M, 4 M and 4.4 M. The composition of the solid phases was checked at different time intervals using ATR-FTIR. The name of the detected phase(s) indicates those time points where the phase was experimentally determined using ATR-FTIR. The coloured backgrounds are areas where the phases occur: gypsum (green), bassanite (orange); both phases (purple).

c(NaCl) /M	1.4	2.4	3.4	3.9	4.4	4.8
Time /h						
0.5	gypsum	gypsum	gypsum	gypsum	gypsum	gypsum
1.0	gypsum	gypsum	gypsum	gypsum	both	bassanite
1.5	gypsum	gypsum	gypsum	gypsum	bassanite	bassanite
2.0	gypsum	gypsum	gypsum	both	bassanite	
2.5	gypsum	gypsum	gypsum	bassanite		
3.0	gypsum	gypsum	gypsum	bassanite		
4.0	gypsum	gypsum	both			
5.0	gypsum	gypsum	both			
6.0	gypsum	gypsum	bassanite			
48	gypsum	gypsum				
272	gypsum	bassanite				

Supporting References

Ashiotis, G., Deschildre, A., Nawaz, Z., Wright, J.P., Karkoulis, D., Picca, F.E., Kieffer, J., 2015. The fast azimuthal integration Python library: pyFAI. J. Appl. Crystallogr. 48, 510–519. https://doi.org/10.1107/S1600576715004306

Beaucage, G., 1995. Approximations Leading to a Unified Exponential/Power-Law Approach to Small-Angle Scattering. J. Appl. Crystallogr. 28, 717–728. https://doi.org/doi:10.1107/S0021889895005292

Besselink, R., Stawski, T.M., Van Driessche, A.E.S., Benning, L.G., 2016. Not just fractal surfaces, but surface fractal aggregates: Derivation of the expression for the structure factor and its applications. J. Chem. Phys. 145, 211908. https://doi.org/10.1063/1.4960953

Eilers, P.H., Boelens, H.F., 2005. Baseline correction with asymmetric least squares smoothing. Leiden Univ. Med. Cent. Rep. 1, 5.

Montes-Hernandez, G., Renard, F., 2016. Time-Resolved in Situ Raman Spectroscopy of the Nucleation and Growth of Siderite, Magnesite, and Calcite and Their Precursors. Cryst. Growth Des. 16, 7218–7230. https://doi.org/10.1021/acs.cgd.6b01406

Parkhurst, D.L., Appelo, C., 2013. Description of input and examples for PHREEQC version 3—a computer program for speciation, batch-reaction, one-dimensional transport, and inverse geochemical calculations. US Geol. Surv. Tech. Methods 6, 497.

Parkhurst, D.L., Appelo, C., 1999. User's guide to PHREEQC (Version 2): A computer program for speciation, batch-reaction, one-dimensional transport, and inverse geochemical calculations. Water-Resour. Investig. Rep. 99, 312.

Peng, J., Peng, S., Jiang, A., Wei, J., Li, C., Tan, J., 2010. Asymmetric least squares for multiple spectra baseline correction. Anal. Chim. Acta 683, 63–68. https://doi.org/10.1016/j.aca.2010.08.033

Rueden, C.T., Schindelin, J., Hiner, M.C., DeZonia, B.E., Walter, A.E., Arena, E.T., Eliceiri, K.W., 2017. ImageJ2: ImageJ for the next generation of scientific image data. BMC Bioinformatics 18, 529. https://doi.org/10.1186/s12859-017-1934-z

Stawski, T.M., Freeman, H.M., Van Driessche, A.E.S., Hövelmann, J., Besselink, R., Wirth, R., Benning, L.G., 2019. Particle-Mediated Nucleation Pathways Are Imprinted in the Internal Structure of Calcium Sulfate Single Crystals. Cryst. Growth Des. 19, 3714–3721. https://doi.org/10.1021/acs.cgd.9b00066

Stawski, T.M., Smales, G.J., Scoppola, E., Jha, D., Morales, L.F.G., Moya, A., Wirth, R., Pauw, B.R., Emmerling, F., Van Driessche, A.E.S., 2021. Seeds of imperfection rule the mesocrystalline disorder in natural anhydrite single crystals. Proc. Natl. Acad. Sci. 118, e2111213118. https://doi.org/10.1073/pnas.2111213118

Stawski, T.M., van Driessche, A.E.S.A.E.S., Ossorio, M., Diego Rodriguez-Blanco, J., Besselink, R., Benning, L.G.L.G., 2016. Formation of calcium sulfate through the aggregation of sub-3 nanometre primary species. Nat. Commun. 7, 11177. https://doi.org/10.1038/ncomms11177

Zizak, I., 2016. The mySpot beamline at BESSY II. J. Large-Scale Res. Facil. JLSRF 2, A102–A102. https://doi.org/10.17815/jlsrf-2-113